



Tailoring Dispersion for Broadband Low-loss Optical Metamaterials Using Deep-subwavelength Inclusions

Zhi Hao Jiang*, Seokho Yun*, Lan Lin, Jeremy A. Bossard, Douglas H. Werner & Theresa S. Mayer

Department of Electrical Engineering and Center for Nanoscale Science, The Pennsylvania State University, 121 Electrical Engineering East, University Park, PA 16802, United States.

SUBJECT AREAS:

METAMATERIALS

TRANSFORMATION OPTICS

NANOPHOTONICS AND
PLASMONICS

MID-INFRARED PHOTONICS

Received
7 December 2012

Accepted
6 March 2013

Published
28 March 2013

Correspondence and requests for materials should be addressed to D.H.W. (dhw@psu.edu) or T.S.M. (tsm2@psu.edu)

* These authors contributed equally to this work.

Metamaterials have the potential to create optical devices with new and diverse functionalities based on novel wave phenomena. Most practical optical systems require that the device properties be tightly controlled over a broad wavelength range. However, optical metamaterials are inherently dispersive, which limits operational bandwidths and leads to high absorption losses. Here, we show that deep-subwavelength inclusions can controllably tailor the dispersive properties of an established metamaterial structure thereby producing a broadband low-loss optical device with a desired response. We experimentally verify this by optimizing an array of nano-notch inclusions, which perturb the mode patterns and strength of the primary and secondary fishnet nanostructure resonances and give an optically thin mid-wave-infrared filter with a broad transmissive pass-band and near-constant group delay. This work outlines a powerful new strategy for realizing a wide range of broadband optical devices that exploit the unique properties of metamaterials.

Metamaterials can be designed to possess remarkable electromagnetic properties including negative^{1,2}, zero/low^{3–5}, and high^{6,7} indices of refraction. These emergent properties, which allow for independent control of the refractive index and the intrinsic impedance, will enable novel optical design strategies with the potential to either greatly improve the performance of existing devices or to introduce entirely new device functionality. Recently, several particularly exciting examples have emerged including ultra-thin absorbers^{8,9}, artificial mirrors¹⁰, electromagnetic induced transparency structures^{11,12}, flat wave collimating lenses¹³, and metasurfaces with customized emission^{14,15}. Fundamentally, the unique optical properties of metamaterials are determined by the specific geometry and arrangement of nanoscale inclusions that are typically aligned in a periodic lattice¹⁶. The resonant properties of these inclusions result in effective refractive indices and group delays that are strongly dependent on wavelength. This dispersive behaviour causes signal distortion and leads to narrow operational bandwidths^{17–20}, which has heretofore limited the widespread use of metamaterials in practical optical devices.

Broadband metamaterials can be realized by creating structures that operate at wavelengths far away from the resonant band of the inclusion to avoid strong dispersion. In the microwave regime, this method has been applied to design ground plane cloaks^{21,22} and Luneburg lenses^{23,24}. However, by avoiding highly dispersive regions, this approach excludes negative and zero/low index values, which are among the most important and potentially rich index regions associated with metamaterials. In contrast to avoiding strongly resonant bands, the dispersive properties of the metamaterial can be exploited by tailoring them to the specific device needs, thereby improving existing components or leading to new optical functionalities^{25–27}. This powerful dispersion engineering design technique has been recently applied to demonstrate novel broadband planar guided-wave devices^{28–30} and radiated-wave components^{31–34} that operate at microwave frequencies.

Despite enormous potential benefits, this design approach has not yet been successfully applied at optical wavelengths because both the electric and magnetic response of the metamaterial must be carefully controlled throughout the entire wavelength band of interest. Achieving this increased level of control leads to significantly more complex nanoscale inclusion geometries and lattice arrangements than are typically found in traditional narrow-band metamaterials. Experimentally realizing optical metamaterials with measured properties that match the theoretically predicted values also requires that the nanofabricated inclusions must accurately reproduce the designed structures⁵. This greatly limits the range of suitable nanostructure inclusions that can be considered in the design process. Therefore, new strategies must be developed to tailor the dispersive properties of metamaterials for broad bandwidth and low loss optical functions, while still meeting the strict constraints imposed by state-of-the-art nanofabrication approaches.



In this paper, we show for the first time that the metamaterial dispersion can be controllably tailored across negative, zero, and positive refractive index values to produce a specific broadband optical function by adding experimentally accessible deep-subwavelength inclusions to a simple metallodielectric fishnet structure. This general design strategy is verified by a specific example - optimizing an optically thin metamaterial band-pass filter with high transmission and nearly constant group delay throughout the 3.0 μm to 3.5 μm midwave infrared (MWIR) spectral window and with high rejection outside this band. To achieve this specific optical function, deep-subwavelength air hole inclusions, which have critical dimensions of less than $1/15 \pm 1/100$ of the shortest design wavelength, are removed from each corner of the larger fishnet air holes to form a modified nano-notched fishnet structure. These inclusions perturb the mode patterns and strength of the unmodified fishnet structure resonances, and shape the effective permittivity and permeability dispersion to simultaneously meet the targeted in-band and out-of-band transmission, rejection, and group delay metrics. The measured optical properties of our nanofabricated free-standing modified metallodielectric fishnet structure are in strong agreement with the simulated values, and confirm that the deep-subwavelength notched inclusions can be produced with the integrity needed for broadband metamaterials. This powerful design approach overcomes the narrow bandwidth limitations of previous optical metamaterials, which dramatically expands the opportunities to create new and practical metamaterial-enabled devices and components.

Results

Tailoring the metamaterial dispersion for a broadband optical response. Our metamaterial design process begins by determining the dispersive effective medium parameters that give a nearly ideal broadband optical band pass filter function with properties approaching those shown in Figure 1a. Along with the ideal in-band transmitted and out-of-band rejected signal power, the transmitted signal also has constant group delay (τ_g) within the pass-band to ensure minimal distortion in its frequency and time domain responses. The metamaterial dispersion is tailored by adjusting the Drude permittivity profile with a plasma wavelength, λ_e , and the permeability profile with Lorentzian resonances on each side of λ_e . Assuming a time dependence of $e^{j\omega t}$, the dispersive effective permittivity (ϵ_{eff}) and permeability (μ_{eff}) models can be expressed in the form,

$$\epsilon_{\text{eff}}(\lambda) = \epsilon_0 \left(\epsilon_\infty - \frac{c_0^2/\lambda_e^2}{c_0^2/\lambda^2 - jc_0\gamma_e/\lambda} \right) \quad (1)$$

$$\mu_{\text{eff}}(\lambda) = \mu_0 \left(1 - \sum_{i=1}^2 \frac{F_i c_0^2/\lambda_e^2}{c_0^2/\lambda^2 - c_0^2/\lambda_{mi}^2 - jc_0\gamma_{mi}/\lambda_{mi}} \right), \quad (2)$$

where c_0 is the speed of light in free space, F_1 and F_2 are the filling factors, γ_e , γ_{m1} and γ_{m2} are the damping factors, and λ_{m1} and λ_{m2} are the wavelengths associated with the two magnetic resonances³⁵.

Realizing this optical metamaterial filter function is achieved by carefully tuning the damping factors, plasma wavelength, and magnetic resonance wavelengths in equations (1) and (2) to simultaneously satisfy all of the desired broadband performance metrics. First, to give a pass-band with nearly ideal transmission, the effective permittivity and permeability must be balanced such that the effective impedance given by,

$$Z_{\text{eff}} = \sqrt{\mu_{\text{eff}}/\epsilon_{\text{eff}}} = Z_0, \quad (3)$$

is matched to free space throughout the targeted pass-band. Outside of this pass-band, the permittivity and permeability are imbalanced (with different signs) to produce an imaginary effective impedance that blocks the transmission of waves. The imaginary parts of the

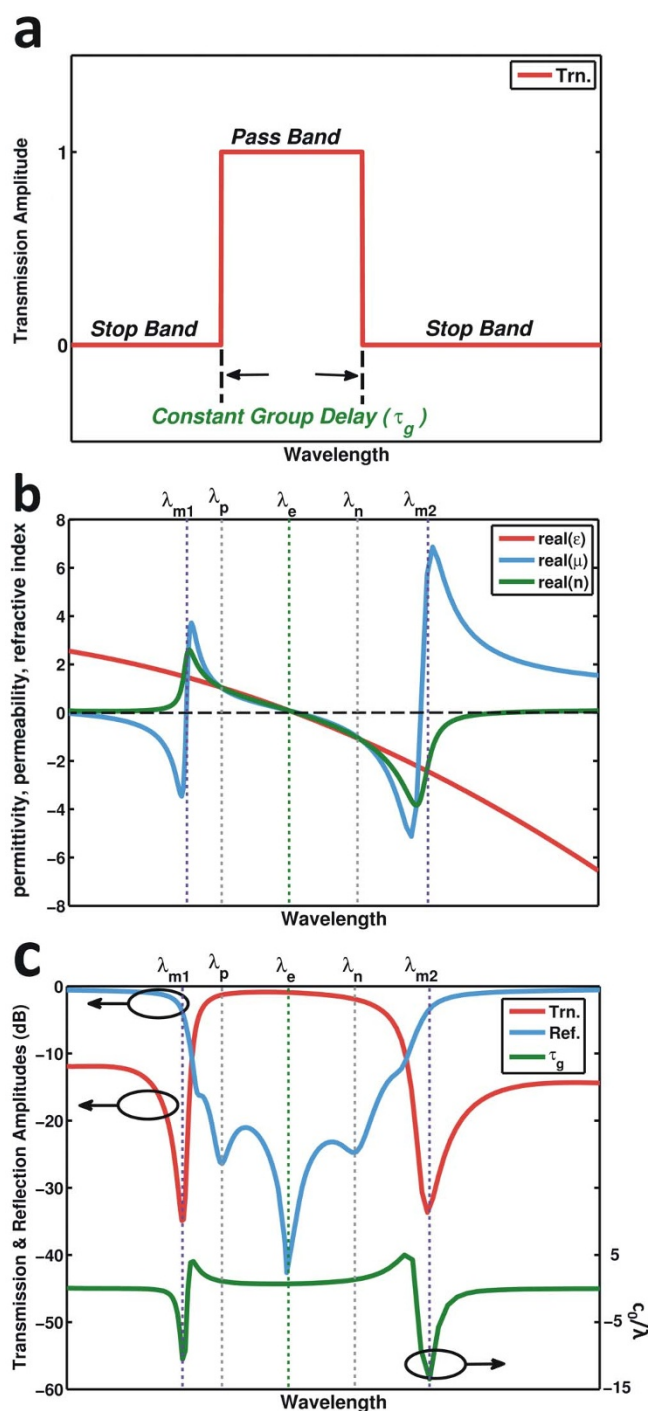


Figure 1 | Target optical metamaterial pass-band filter with matched in-band permittivity and permeability dispersion. (a) Ideal response of the band pass filter with a flat transmission window and a flat group delay within the pass-band. (b) Real parts of the dispersive permittivity (red), permeability (blue) and refractive index (green) properties of this material. (c) The transmission (red), reflection (blue) and group delay τ_g (green) of a slab of this metamaterial with a thickness of $0.15\lambda_e$.

permittivity and permeability are not considered here for simplicity. However, it should be noted that the metamaterial absorption loss must also be suppressed to ensure a high transmission. Second, a nearly constant group delay is enforced across the pass-band by setting,



$$\tau_g = \frac{L}{v_g} = \frac{L \left(\text{Re}(n_{\text{eff}}) + \omega \frac{d(\text{Re}(n_{\text{eff}}))}{d\omega} \right)}{c_0} = \text{constant}, \quad (4)$$

where v_g is the group velocity, c_0 is the speed of light in free space, L is the total thickness of the material slab, and n is the effective index of refraction. Therefore, the slopes of the permittivity, the permeability, and the resulting refractive index profiles must also be properly controlled to give $\text{Re}(n_{\text{eff}}) + \omega d(\text{Re}(n_{\text{eff}}))/d\omega = \text{constant}$ throughout the band.

This multiple parameter design objective is satisfied by the dispersive metamaterial properties displayed in Figure 1b, which result in an effective refractive index that gradually changes from positive to negative values with increasing wavelength. Between the wavelengths corresponding to a negative unity and positive unity refractive index (*i.e.*, between λ_n and λ_p), the values of the permittivity, permeability, and refractive index along with their slopes are balanced to meet both of the in-band design objectives. Figure 1c shows the simulated transmission and reflection amplitudes and the group delay for a uniform $\sim 0.15\lambda_c$ thick slab of this broadband metamaterial, which exhibits a highly transmissive 1 dB pass-band with a near-constant group delay between λ_n and λ_p . In comparison with conventional optical filter design approaches that focus on shaping the transmission and reflection amplitudes, our approach includes control over the group delay by tailoring the dispersion of the effective medium properties, which contain the transmission and reflection phase information as well.

Broadband metamaterial design using deep-subwavelength inclusions. The next step in our broadband optical metamaterial design process was to identify a metallodielectric nanostructure that produces the dispersive properties shown in Figure 1b and that is also compatible with large-area nanofabrication. In this work, we selected a filter with a 1 dB pass-band in the MWIR between 3.0 μm and 3.5 μm , and stop bands on either side of the pass-band extending down to 2.5 μm and up to 4.0 μm . We began with a conventional fishnet nanostructure composed of a three-layer metal-dielectric-metal stack perforated with a doubly periodic array of air holes because this structure provides greater flexibility to adjust the effective permittivity and permeability from positive to negative values^{2,5,36,37}. Deep sub-wavelength notch load inclusions were added to each corner of the square air holes to precisely control the metallic strip permittivity dilution percentage as well as the wavelength and strength of both the primary and secondary magnetic resonances. This gives extremely fine control of both the effective permittivity and permeability dispersion as will be discussed in following Sections.

A genetic algorithm (GA) technique³⁸ coupled with an efficient full-wave electromagnetic solver was employed to optimize the modified fishnet nanostructure dimensions for the effective medium parameter dispersion required to meet the challenging multi-objective design criteria. Importantly, predefined constraints on the allowable unit cell size, air hole size, nano-notch size, and layer thicknesses were incorporated into the optimization algorithm to avoid generating structures that are impractical to fabricate³⁹. Eight-fold symmetry was enforced on the structure in the plane perpendicular to the incident wave vector to ensure a polarization insensitive response for normally incident plane waves. Finally, experimentally measured dispersive optical properties for the constituent metal and dielectric materials were used in the full-wave solver to minimize discrepancies between the simulated and experimentally fabricated metamaterial response.

For each candidate design in the GA optimization, the complex transmission and reflection coefficients were calculated using Ansoft High Frequency Structure Simulator⁴⁰ (HFSS) finite-element solver. Periodic boundary conditions were assigned to the lateral walls of the

simulation domain to approximate a plane wave normally incident on the structure. The effective medium parameters (ϵ_{eff} , μ_{eff}) within the target wavelength range were retrieved from the transmission and reflection coefficients by using an inversion algorithm⁴¹. These parameters were compared with the target effective medium requirements to determine the *Cost* of the candidate design, which is defined by

$$\left\{ \begin{array}{l} \text{Cost 1} = \sum_{\lambda_{n,e,p}} \left[\left| \epsilon_{\text{eff}} - \epsilon_{\text{tar},i} \right| + \left| \mu_{\text{eff}} - \mu_{\text{tar},i} \right| \right] + \\ \sum_{\lambda_{\text{stop}}} \left[\frac{1}{\log(Z_{\text{eff}})} \right] \\ \text{Cost 2} = \sum_{\lambda_{\text{pass}}} \left[\left| \tau_g - \tau_{g,\text{mean}} \right| \right] \end{array} \right. \quad (5)$$

$$\text{Cost} = \text{Cost 1} + \text{Cost 2} \quad (6)$$

where $\epsilon_{\text{tar},i} = \{-1, 0, 1\}$ and $\mu_{\text{tar},i} = \{-1, 0, 1\}$ are the targeted permittivity and permeability values at λ_n , λ_e , and λ_p , respectively, λ_{stop} refers to the wavelength range larger than λ_n and smaller than λ_p , and $\tau_{g,\text{mean}}$ is the average group delay of the sample frequency points within the pass-band. *Cost1* minimizes the difference between the targeted and optimized values for permittivity and permeability in the pass-band and maximizes the impedance mismatch at the stop band frequencies to ensure high reflection. It also minimizes the absorption loss, *i.e.*, the imaginary parts of permittivity and permeability, of the metamaterial. *Cost2* minimizes the group delay variation in the pass-band. The GA evolved solutions until it converged on a metallodielectric nanostructure with a sufficiently low overall *Cost* value that met the target design criteria specified in Figure 1b,c.

A single unit cell of the modified fishnet nanostructure with the optimized dimensions is shown in Figure 2a. In this design, Au was used for the top and bottom metal layers, and polyimide served as the intermediate dielectric layer. The period p of the square unit cell is 2113 nm, and the side w of the primary fishnet square air hole is 990 nm. Each corner of the fishnet air hole is loaded with two deep-sub-wavelength square air hole notches that are 198 nm on a side. As discussed in later sections, changes of more than ± 30 nm (equivalent to $\lambda_p/100$) in the nano-notch dimensions result in significant deviations from the targeted dispersive effective medium parameters, and thus the metamaterial filter response. This emphasizes the importance of properly optimizing the deep-subwavelength inclusions for achieving a pre-defined broadband optical response. Finally, the total thickness of the three-layer metallodielectric stack is 510 nm, which is less than $0.16\lambda_c$ at the center wavelength of the pass-band (*i.e.*, 3.25 μm). Specifically, the top and bottom Au layers were 30 nm thick, and the polyimide layer was 450 nm thick. Such thin metamaterial-enabled broadband devices could provide an alternative to conventional thick multilayer stacks or complex three-dimensional nanostructures for integrated nano- or micro-scale optical systems^{42–45}.

Simulated optical properties of the broadband metamaterial filter.

The simulated optical response and effective medium properties of the optimized modified fishnet nanostructure are shown in Figure 3a,b. Within the target 1 dB pass-band between 3.0 μm and 3.5 μm , the average transmitted power at normal incidence is 82% (-0.9 dB), while the average reflected and absorbed power are 4% and 14%, respectively. Notably, the maximum variation in transmitted power is less than 9% (0.4 dB) across the full pass-band window, which confirms that this structure provides excellent control of the effective medium parameters across a broad bandwidth (Fig. 3a, top). Such a high value of transmittance over a broad wavelength range has not been previously demonstrated in optical and plasmonic metamaterials^{2,36,42,46–49}. Outside the pass-band, the mismatched impedance to free-space results in a high reflectivity (Fig. 3a, middle), which reduces the average transmitted power to

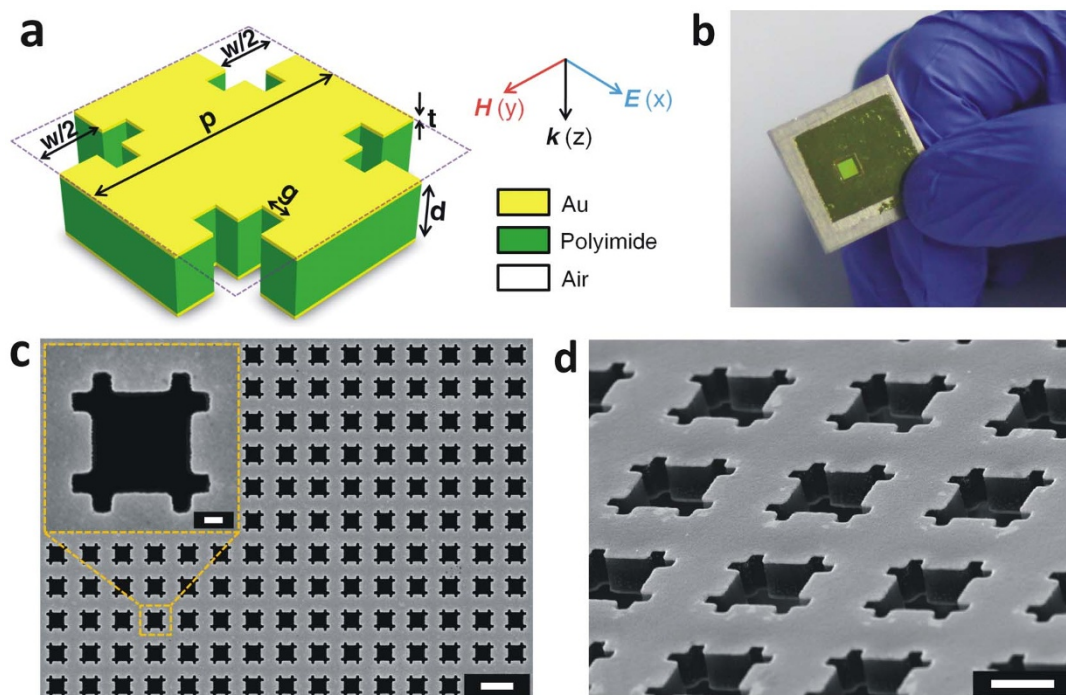


Figure 2 | Broadband optical metamaterial band pass filter design. (a) The geometry and dimensions of a single unit cell of the modified fishnet nanostructure. The optimized geometry dimensions are $p = 2113$ nm, $w = 990$ nm, $g = 198$ nm, $t = 30$ nm and $d = 450$ nm. (b) A photograph of the fabricated free-standing metamaterial mounted on an Al frame. (c) Top-view FESEM image of a portion of the freestanding nanofabricated modified fishnet nanostructure. Scale bar: 3 μm . The inset shows the magnified top view of a single unit cell. Scale bar: 200 nm. Reproducing the deep-subwavelength nano-notch features is critical to achieving the optimized optical properties in the fabricated structure. (d) Tilted view FESEM image of the nanostructure with nearly vertical (89°) side walls. Scale bar: 1 μm .

less than 10% (-10 dB). Here, the average reflected power is 71%, while the average absorbed power is 19%. The higher value of out-of-band absorption is attributed to absorption from the two magnetic resonances, which are positioned at wavelengths corresponding to the edges of the pass-band. The transition between the pass-band and the stop bands have steep roll-offs of ~ 93 dB μm^{-1} on the short wavelength side and ~ 101 dB μm^{-1} on the long wavelength side.

The simulated group delay of this modified fishnet structure is also plotted in Figure 3a, and it exhibits a small variation from 15 fs to 27 fs across the transmission pass-band window from 3.0 μm to 3.5 μm . This group delay fluctuation of ~ 1 period within a 20% bandwidth is much lower than has been previously reported for negative index metamaterials^{36,46}, which had fluctuations of ~ 3 periods within a 5% bandwidth. In addition, the simultaneously negative

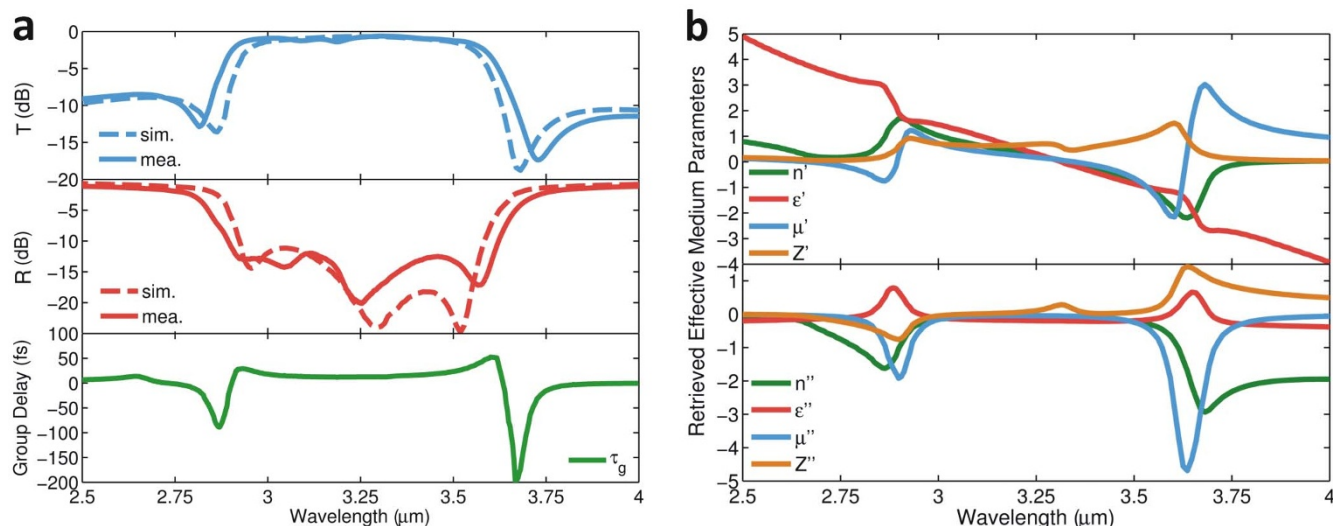


Figure 3 | Simulated and measured optical properties and effective medium parameters of the fabricated modified fishnet nanostructure. (a) Simulated and measured transmission (top, blue) and reflection (middle, red) magnitudes for normally incident radiation showing broadband transmission over the highlighted region from 3.0 μm to 3.5 μm . Simulated group delay τ_g (bottom) shows minimal variation over the transmission window. (b) Real (top) and imaginary (bottom) parts of the effective index of refraction n_{eff} (green), permittivity ϵ_{eff} (red), permeability μ_{eff} (blue), and impedance Z_{eff} (orange) retrieved from the full-wave simulation of the metamaterial structure. The real parts of ϵ_{eff} and μ_{eff} follow a similar slope from 3.0 μm to 3.5 μm , indicating a matched impedance, whereas the imaginary parts are small, indicating low intrinsic losses.



phase and group velocities can also be identified within the range from 3.65 μm to 3.70 μm , which corroborates a previously reported result³⁶. From these results, we expect that even better control over the effective medium parameter profiles and resulting broadband optical properties could be achieved given additional geometric design flexibility, at the expense of more challenging nanofabrication requirements.

Simulated effective medium parameters of the broadband metamaterial filter. The optical properties of the modified fishnet nanostructure can be understood by examining the simulated effective permittivity, permeability, refractive index, and impedance shown in Figure 3b. Although these effective medium parameters are nonlocal in nature⁵⁰, they offer insight into how the electric and magnetic responses of the designed nanostructure vary with wavelength. The primary magnetic resonance of the conventional fishnet structure has been widely exploited to produce a narrow negative effective refractive index band^{1,2,36}. In this work, we added the deep subwavelength nano-notched inclusions to shape the effective permeability dispersion by customizing the strength and wavelength of both the primary and secondary magnetic resonance modes. These same inclusions were used to tailor the slope and plasma wavelength of the effective permittivity, which is governed by the air hole waveguide array cut-off (see Supplementary Information for a comparison of fishnet structures with and without these inclusions).

The dispersive properties of the optimized metamaterial shown in Figure 3b agree well with the targeted effective medium parameters in Figure 1b. The effective permeability has a strong primary magnetic resonance at 3.70 μm and a weaker secondary resonance at 2.85 μm , which correspond to the transmission minima of the filter. The relative strengths of these two resonances give a nearly linear decreasing effective permittivity that varies from $\mu_{\text{eff}} = +0.95$ at $\lambda_p = 3.0$ μm to $\mu_{\text{eff}} = -0.90$ at $\lambda_n = 3.5$ μm , with a zero crossing at $\lambda_e = 3.25$ μm . In contrast to the targeted properties, the effective permittivity of the modified fishnet structure exhibits two small anti-resonances⁵¹ that are caused by the magnetic resonance modes. These anti-resonances introduce a slightly larger discrepancy in the effective permittivity and permeability profiles than the targeted design values, producing an optimized permittivity that varies from $\epsilon_{\text{eff}} = +1.20$ to $\epsilon_{\text{eff}} = -0.95$ across the same wavelength range. Despite the small differences, the effective impedance of this structure is well-matched to free-space throughout the entire pass-band, providing for its low reflectance across this band. Outside the pass-band the impedance is purely imaginary, which appears to be inductive in the long wavelength range and capacitive in the short wavelength regime. This impedance mismatch is responsible for the strong reflection in the stop-bands. Finally, the effective refractive index, which decreases from $n_{\text{eff}} = +1.05$ at $\lambda_p = 3.0$ μm to $n_{\text{eff}} = -0.92$ at $\lambda_n = 3.5$ μm , has a dispersive rate of change (*i.e.*, slope) that compensates for the refractive index dispersion and produces the nearly constant group delay.

Although not shown in Figure 1b, the imaginary parts of the permittivity, permeability, and refractive index must be minimized throughout the transmission band to ensure the metamaterial has low absorption loss. Therefore, the cost function used for the GA included this constraint when optimizing the geometry and dimensions of the modified fishnet structure. The effective medium properties plotted in Figure 3b show that the imaginary part of effective refractive index has a magnitude less than 0.15 across the entire pass-band. This leads to the low broadband absorption loss for light passing through the modified fishnet structure. Additionally, our structure lacks the sharp evanescent mode gap^{51,52} observed in metamaterials that realize the near-zero refractive index condition by allowing either the permittivity or permeability to approach zero alone. This condition produces a purely imaginary effective

impedance that blocks the transmission of light. In contrast, the impedance matched zero-index band of our structure possesses a non-vanishing group velocity, and yields high transmission across the band. This is an optical analogue to the balanced transmission-line metamaterial proposed for applications in the microwave range^{25,26}.

Resonant electromagnetic response of the broadband metamaterial filter. The resonant electromagnetic response that generates the desired broadband filtering properties can be understood by analyzing the volumetric current density and magnetic field distributions plotted in Figure 4. It has been shown previously that the primary and secondary magnetic resonance modes of conventional tri-layer fishnet nanostructures can be attributed to anti-parallel currents induced on the top and bottom metal layers by excited gap surface plasmon polaritons (gap-SPPs) propagating along the central dielectric slab⁵³. In particular, the incident light is coupled into the gap-SPP modes when the parallel momentum provided by the nanostructure periodicity is equal to that of the SPPs, *i.e.*, $k_{\text{spp}} = iG_x + jG_y$ for normal incidence, where $G_x = G_y = 2\pi/p$. For the fundamental magnetic resonance mode of our modified fishnet structure at 3.7 μm , the anti-parallel currents flow primarily in the x direction (Figure 4a,b, left), with a phase difference of 180° between the highlighted central rectangular area and the outer area of the unit cell. This produces thin rectangular charge accumulation and depletion regions near the boundaries of the highlighted region with different current phases, which indicates that displacement currents are present between the two metal layers. Orthogonal to the current on the two metal layers, the magnetic field points mainly in the y direction (Figure 4c, left) with almost no variation along the y -axis, and exhibits a 180° phase difference in the highlighted central region, as compared to the surrounding areas. This dipole-like magnetic field pattern corresponds to the $(i,j) = (1,0)$ SPP mode.

In contrast to the primary magnetic resonance, the current distribution for the secondary resonance at 2.85 μm creates charge accumulation and depletion in two small point-like regions at the two ends of the line dividing the highlighted central rectangular area of the unit cell (Figure 4a,b, right). This leads to a curl-type distribution of the magnetic fields due to the linear displacement current between the metal layers in these regions (Figure 4c, right). Two quadrupole-like magnetic field patterns can be identified at the center of the two highlighted square regions in the magnetic field distribution. The magnetic field patterns possess two nodes per period along the y -axis, indicating that the higher order $(i,j) = (1,1)$ SPP mode is efficiently excited. When compared to the fundamental mode at 3.7 μm , this higher order SPP mode is weaker in terms of the magnetic field intensity, thus resulting in a weaker resonance in the permeability with a lower quality factor, as seen in Figure 3b.

Importance of the deep-subwavelength inclusions. As illustrated in Figure 4, the deep subwavelength nano-notch inclusions perturb the current distribution and magnetic field of the conventional fishnet structure, which modifies the wavelength and strength of the gap-SPP enabled magnetic resonances, as well as the plasma wavelength of the air hole waveguide array. A detailed parametric study that analyzes the effect of the nano-notch inclusions on the broadband metamaterial properties and the effective medium parameters is provided in Figure 5. These results show that removing the nano-notch inclusions from the modified fishnet structure converts the high transmittance 1 dB pass-band window into a much wider stop-band, with a high average reflected power of 85% (-0.7 dB) across the 3.0 μm to 3.5 μm wavelength range. This dramatic difference in the optical properties of the metamaterial is due to the large change in resonance wavelength and slope of the effective permittivity and permeability parameter profiles. Further study re-optimizing the dimensions of the conventional fishnet nanostructure to meet the

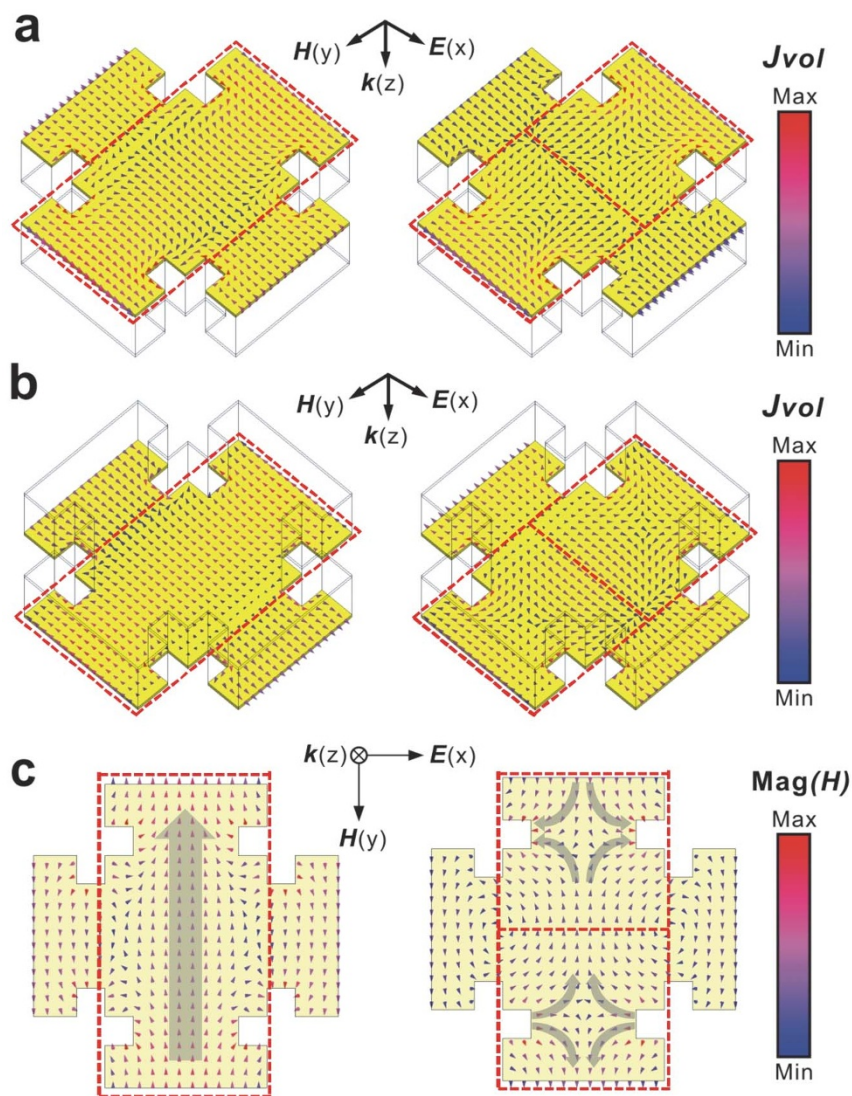


Figure 4 | Volumetric current density and magnetic field distributions of the modified fishnet nanostructure at the two magnetic resonance modes. (a) Volumetric current density distribution on the top Au layer at 3.70 μm (left) and 2.85 μm (right). (b) Volumetric current density distribution on the bottom Au layer at 3.70 μm (left) and 2.85 μm (right). (c) Top-view of the magnetic field distribution in the structure at 3.70 μm (left) and 2.85 μm (right).

metamaterial filter design criteria reveals that the lack of subwavelength nano-notches places appreciable limits on the best filter performance that can be obtained (see Supplementary Information).

The effect of varying the nano-notch sidewall length from $g = 138$ to 258 nm in 30 nm increments around the optimized value of $g = 198$ nm is also presented in Figure 5. Notably, increasing or decreasing critical feature size of the nano-notches by only ± 30 nm (equivalent to $\sim \lambda_p/100$) from the optimized value results in a significant reduction in the average pass-band transmission of 82% down to 69% for $g = 168$ nm and 64% for $g = 228$ nm (Figure 5a). In addition, the 0.5 μm bandwidth of the 1 dB pass-band window increased by 1000 nm for $g = 168$ nm and decreased by 800 nm for $g = 228$ nm. Even larger deviations from the optimized transmission, reflection, and bandwidth are observed for the smallest and largest nano-notch dimensions studied here. Similar trends in variability and bandwidth are observed in the group delay of the metamaterial (Figure 5b).

Figure 5c,d shows that variations in nano-notch critical feature size equivalent to $\sim \lambda_p/100$ have a large effect on the effective permittivity and permeability dispersion across the wavelength band of interest. This is because the air-hole waveguide array cut-off wavelength and the gap-SPP propagation are both strongly dependent on

the deep subwavelength inclusions. Specifically, the effective plasma wavelength of the modified fishnet structure increases from a value of $\lambda_{plasma} = 3.0$ μm when $g = 138$ nm to $\lambda_{plasma} = 3.6$ μm when $g = 258$ nm. Additionally, the anti-resonance associated with the fundamental magnetic resonance mode becomes weaker with increasing g , which reduces the wavelength dependence in the effective permittivity for structures with larger nano-notches. In contrast, the primary magnetic resonance becomes significantly stronger, while the secondary resonance becomes weaker and shifts to longer wavelengths, with increasing g . Thus, the effective permeability becomes more dispersive as the nano-notch size is increased. The dependence of structural resonances on small geometrical variations revealed here also corroborates a previous study on the resonance positioning of plasmonic particles based on geometrical perturbation⁵⁴.

Experimental realization and characterization. The optimized modified fishnet metamaterial structure was fabricated by defining the nano-notched air hole array shown in Figure 2b in the three-layer metalodielectric structure using top-down nanofabrication methods⁵ (see Methods). Briefly, the Au-polyimide-Au stack and an additional SiO₂ hard mask layer were deposited on a thermally oxidized Si handle substrate. The nano-notched air holes were patterned by

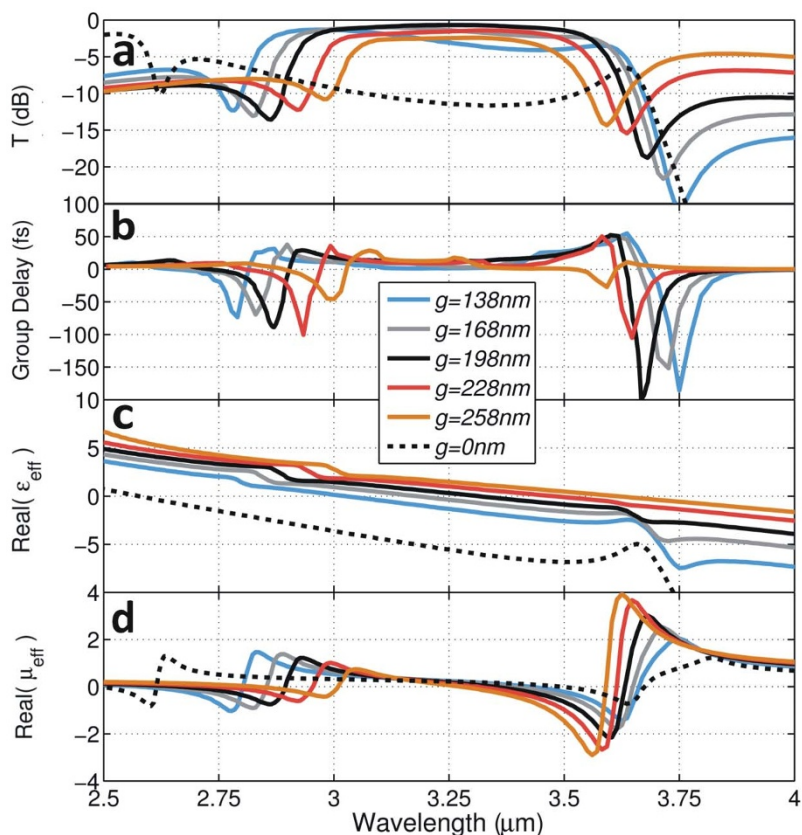


Figure 5 | Numerical parametric analysis of the modified fishnet nanostructure with various nano-notch inclusion sizes. (a) Transmission amplitude. (b) Group delay. (c) Effective permittivity. (d) Effective permeability.

electron-beam lithography, and then transferred through the material stack using high-aspect-ratio reactive ion etching (RIE). The modified fishnet nanostructure was completed by removing the electron-beam resist and the SiO₂ hard mask. To prevent degradation in optical properties due to substrate-induced bianisotropy⁵⁵, the optically thin structure was released from the handle substrate by selective etching of thermal oxide and then mounted on a frame for optical characterization.

Figure 2c,d show field emission scanning electron microscope (FESEM) images of the top surface of the freestanding modified fishnet nanostructure taken without tilt (Figure 2c) and with a 30° tilt (Figure 2d). The critical dimensions of the air hole features were measured on the top and bottom surfaces of the released structures positioned at normal incidence (no tilt) with respect to the electron beam. The large air hole had $w = 1000$ nm on the top surface, and 980 nm on the bottom surface. The nano-notch sidewall length was $g = 195$ nm on the top surface, and 175 nm on the bottom surface, with an average of 185 nm. These measurements confirm that the fabricated modified fishnet structure reproduces the design geometry with an ~5% deviation in the average nano-notch sidewall length from the optimized value. From simulation, this small difference in g should not have a significant effect on the metamaterial optical properties.

The sidewall angle determined from the difference between the measured top and bottom nano-notch sidewall lengths is 89°. This is significantly higher than the 79° sidewall angles of similar multilayer fishnet structures fabricated by lift-off and focused ion beam etching processes^{2,47,56,57}. The latter processes would result in fully closed nano-notches at the backside of the structure, and give an average sidewall length of $g = 100$ nm. As revealed in Figure 5, this deviation from the design target would significantly degrade the optical properties of the optimized modified fishnet nanostructure. Thus, the

high aspect ratio patterning and etching process demonstrated here is essential to our experimental validation of this design approach. The nearly ideal vertical sidewall profile of our structure also minimizes sidewall-angle induced magneto-electric coupling, which is another source of bianisotropy that degrades the performance of most metallo-dielectric optical metamaterials⁵⁶.

The nanofabricated freestanding modified fishnet structure was characterized using a Fourier transform infrared (FTIR) spectrometer equipped with a custom optical setup to obtain transmission and reflection at normal incidence (see Methods). The measured optical properties shown in Figure 3a are in strong agreement with the simulation results, exhibiting a high and flat in-band transmission as well as a high out-of-band reflection. The average transmitted power within the experimentally measured 1 dB pass-band window from 2.95 μm to 3.60 μm is 80% (−1.0 dB), while the average in-band reflected and absorbed power are 4% and 16%, respectively. Additionally, the transmission window of the fabricated structure has a maximum variation of only 11% (0.5 dB) over the entire pass-band, which confirms that the impedance match is maintained as the index traverses zero. The average transmitted power in the short and long wavelength stop-band regions remain below 12% (−9.2 dB) and 8% (−11 dB), respectively. This gives an average transmitted power across both stop-bands of approximately 10% (−10.1 dB), with an average reflected power of 64% and average absorbed power of 26%. The roll-off rates between the pass-band and stop-band on the short and long wavelength sides are 76 dBμm^{−1} and 91 dBμm^{−1}, respectively.

From the results in Figure 3, only small discrepancies are observed in the measured bandwidth, roll-off rates, and transmittance of the fabricated modified fishnet structure relative to the simulated values of the optimized structure. Specifically, the measured bandwidth of the 1 dB transmission window is 0.15 μm wider than the designed



range, extending from 2.95 μm to 3.60 μm as compared with 3.0 μm to 3.5 μm . The roll-off rates of the short and long wavelength edges of the pass-band are decreased from the predicted 93 $\text{dB}\mu\text{m}^{-1}$ and 101 $\text{dB}\mu\text{m}^{-1}$ to the measured 76 $\text{dB}\mu\text{m}^{-1}$ and 91 $\text{dB}\mu\text{m}^{-1}$. Finally, there is a slight decrease in average in-band transmitted power from 82% to 80%, which is due to a $\sim 2\%$ increase in the absorption in the fabricated structure. The slightly increased bandwidth, decreased roll-off rates, and higher absorption are caused by the slightly smaller nano-notch size and the lower quality factor of the resonances within the band (see Figure 3a transmission and reflection curves). We attribute the lower quality factor to several nanofabrication related aspects, including the rounded corners of the nano-notch as well as small deviations in the structure dimensions (*e.g.*, layer thicknesses and air hole size) and the constitutive material properties from the values used in the simulation. Despite these slight deviations from the ideal performance, this strong agreement between experimental and simulated optical properties validates this design concept, and shows that deep-subwavelength inclusions can be used to tailor the permittivity and permeability dispersion for broadband performance.

Discussion

In summary, we have demonstrated a new approach for realizing low-loss optical metamaterials with a predefined broadband response by adding deep-subwavelength inclusions to shape the metamaterial dispersion. We validated this technique by designing and fabricating an optically thin MWIR pass-band metamaterial filter with high in-band transmission and out-of-band rejection as well as nearly constant in-band group delay. To achieve this complex optical response, the effective permittivity and permeability were matched throughout the pass-band and were purposely imbalanced outside of this band. The refractive index dispersion and its slope were also constrained to provide the near-constant group delay, which varied from a $n_{\text{eff}} \sim +1$ to $n_{\text{eff}} \sim -1$ at the edges of the 1 dB pass-band window.

Our optimized broadband optical metamaterial filter was experimentally implemented using deep-subwavelength nano-notch inclusions to controllably perturb the primary and secondary resonances of a conventional fishnet nanostructure. Theoretical analysis showed that varying the $\pm \lambda_p/15$ nano-notch inclusion dimensions by $\pm \lambda_p/100$ had a marked effect on both the strength and the position of these resonances, and provided the flexibility needed to tailor the dispersion of each effective medium parameter over the broad wavelength range. The nanofabricated free-standing modified fishnet structure replicated the optimized design geometry to within $\sim 5\%$ of the targeted dimensions. Optical measurements of this structure were in strong agreement with the simulated properties, and demonstrated a 1 dB pass-band window between 2.95 μm and 3.60 μm with an average transmitted power of $>80\%$ and a maximum variation of 11%. The average transmitted power measured outside of the pass-band was $<10\%$. Moreover, a nearly constant group delay was achieved with a small variation of <12 fs. This demonstration confirms that deep-subwavelength inclusions can be used to controllably tailor metamaterial dispersion, and this general approach paves the way for an array of new broadband optical devices that exploit the unique properties offered by metamaterials.

Methods

Device fabrication. The nanofabrication process began by depositing the tri-layer Au-polyimide-Au stack and a SiO_2 masking layer on a thermally oxidized Si handle substrate. The 30 nm thick top and bottom Au layers were evaporated at a rate of 1.5 \AA s^{-1} using e-beam evaporation (Kurt Lesker LAB-18), and the 450 nm thick intermediate dielectric layer was deposited by spin-coating a polyimide precursor (HD Microsystem PI2556 resin diluted by 50% using HD Microsystem T9039 polyimide thinner) at a speed of 3000 rpm for 40 seconds. The as-spun polyimide layer was fully imidized by first heating at 150°C for 30 minutes and then at 250°C for 1 hour in a nitrogen-purged convection oven. A 220 nm thick SiO_2 hard mask layer

was then deposited onto the top Au layer using Plasma Enhanced Chemical Vapor Deposition (Applied Materials P-5000).

A 300 nm thick layer of positive electron-beam resist (ZEON ZEP 520A) was applied with a spin speed of 5000 rpm for 1 minute, followed by a soft bake at 180°C for 3 minutes. The nano-notch loaded square air hole array was patterned using electron-beam lithography (Leica EBPG5-HR) with a dose of $180 \mu\text{C}/\text{cm}^2$ and beam spot size of 43 nm. The exposed pattern was developed in *n*-amyl acetate for 3 min and rinsed in MIBK:IPA (8:1) for 1 min. The developed resist pattern was first transferred into the SiO_2 layer by magnetically enhanced reactive ion etching (MERIE) using a CHF_3 and CF_4 plasma (Applied Materials P-5000), and then into the tri-layer stack using sequential RIE processes. A Cl_2 -based inductively coupled plasma was used to etch the top and bottom Au layers (PlasmaTherm Versalock 700), and an O_2 -based magnetically enhanced plasma was used to etch the polyimide spacer (Applied Materials P-5000). The remaining SiO_2 hard mask layer was removed using a low-power F-based plasma process. The fabricated metamaterial structure was removed from the sacrificial substrate by etching the underlying thermal oxide using buffered oxide etchant, and it was mounted on an Al frame for optical characterization.

Optical characterization. The freestanding metamaterial filter was characterized using a Fourier transform infrared (FTIR) spectrometer (Bruker Optics IFS-66) equipped with a liquid nitrogen cooled mercury cadmium telluride detector. The transmission and reflection amplitudes were measured at normal incidence. For the reflection measurement, a custom optical setup composed of mirrors and a beam splitter was mounted in the main compartment of the FTIR to collect the specular reflection at normal incidence. The absolute transmission amplitude was calculated by normalizing the measured spectrum to an air background, and the absolute reflection amplitude was determined by referencing the measured values to the reflectivity of an Au mirror.

- Shelby, R. A., Smith, D. R. & Schultz, S. Experimental verification of a negative index of refraction. *Science* **292**, 77–79 (2001).
- Valentine, J. *et al.* Three-dimensional optical metamaterial with a negative refractive index. *Nature* **455**, 376–379 (2008).
- Edwards, B., Alù, A., Young, M. E., Silveirinha, M. & Engheta, N. Experimental verification of epsilon-near-zero metamaterial coupling and energy squeezing using a microwave waveguide. *Phys. Rev. Lett.* **100**, 033903 (2008).
- Kocaman, S. *et al.* Zero phase delay in negative-refractive-index photonic crystal superlattices. *Nat. Photon.* **5**, 499–505 (2011).
- Yun, S. *et al.* Low-loss impedance-matched optical metamaterials with zero-phase delay. *ACS Nano* **6**, 4475–4482 (2012).
- Shin, J., Shen, J. T. & Fan, S. Three-dimensional metamaterials with an ultrahigh effective refractive index over a broad bandwidth. *Phys. Rev. Lett.* **102**, 093093 (2009).
- Choi, M. *et al.* A terahertz metamaterial with unnaturally high refractive index. *Nature* **470**, 369–373 (2011).
- Landy, N. I., Sajuyigbe, S., Mock, J. J., Smith, D. R. & Padilla, W. J. Perfect metamaterial absorber. *Phys. Rev. Lett.* **100**, 207402 (2008).
- Jiang, Z. H., Yun, S., Toor, F., Werner, D. H. & Mayer, T. S. Conformal dual-band near-perfectly absorbing mid-infrared metamaterial coating. *ACS Nano* **5**, 4641–4647 (2011).
- Brian, T. & Piestun, R. Total external reflection from metamaterials with ultralow refractive index. *J. Opt. Soc. Am. B* **20**, 2448–2453 (2003).
- Zhang, S., Genov, D. A., Wang, Y., Liu, M. & Zhang, X. Plasmon-induced transparency in metamaterials. *Phys. Rev. Lett.* **101**, 047401 (2005).
- Liu, N. *et al.* Plasmonic analogue of electromagnetic induced transparency at the Drude damping limit. *Nat. Mater.* **8**, 758–762 (2009).
- Enoch, S., Tayeb, G., Sabouroux, P., Guérin, N. & Vincent, P. A metamaterial for directive emission. *Phys. Rev. Lett.* **89**, 213902 (2002).
- Liu, X. *et al.* Taming the blackbody with infrared metamaterials as selective thermal emitters. *Phys. Rev. Lett.* **107**, 045901 (2011).
- Bossard, J. A. & Werner, D. H. Metamaterials with custom emissivity polarization in the near-infrared. *Opt. Express* **21**, 3872–3884 (2013).
- Koschny, T., Kafesaki, M., Economou, E. N. & Soukoulis, C. M. Effective medium theory of left-handed materials. *Phys. Rev. Lett.* **93**, 107402 (2004).
- Grbic, A. & Eleftheriades, G. V. Overcoming the diffraction limit with a planar left-handed transmission-line lens. *Phys. Rev. Lett.* **92**, 117403 (2004).
- Fang, N., Lee, H., Sun, C. & Zhang, X. Sub-diffraction-limited optical imaging with a silver superlens. *Science* **308**, 534–537 (2005).
- Schurig, D. *et al.* Metamaterial electromagnetic cloak at microwave frequencies. *Science* **314**, 977–980 (2006).
- Cai, W. S., Chettiar, U. K., Kildishev, A. V. & Shalaev, V. M. Optical cloaking with metamaterials. *Nat. Photon.* **1**, 224–227 (2007).
- Liu, R. *et al.* Broadband ground-plane cloak. *Science* **323**, 366–369 (2009).
- Valentine, J., Li, J., Zentgraf, T., Bartal, G. & Zhang, X. An optical cloak made of dielectrics. *Nat. Mater.* **8**, 568–571 (2009).
- Kundtz, N. & Smith, D. R. Extreme-angle broadband metamaterial lens. *Nat. Mater.* **9**, 129–132 (2010).
- Ma, H. F. & Cui, T. J. Three-dimensional broadband and broad-angle transformation-optics lens. *Nat. Commun.* **1**, 124 (2010).



25. Caloz, C. & Itoh, T. *Electromagnetic Metamaterials: Transmission Line Theory and Microwave Applications* (John Wiley-IEEE Press, 2005).
26. Eleftheriades, G. V. & Balmain, K. G. *Negative Refraction Metamaterials: Fundamental Principles and Applications* (Wiley-IEEE Press, 2005).
27. Zhudlev, N. I. The road ahead for metamaterials. *Science* **328**, 582–583 (2010).
28. Antoniadis, M. A. & Eleftheriades, G. V. A broadband series power divider using zero-degree metamaterial phase-shifting lines. *IEEE Microw. Wireless Compon. Lett.* **15**, 808–810 (2005).
29. Okabe, H., Caloz, C. & Itoh, T. A compact enhanced-bandwidth hybrid ring using an artificial lumped-element left-handed transmission-line section. *IEEE Trans. Microw. Theory Tech.* **52**, 798–804 (2004).
30. Gupta, S. & Caloz, C. Analog signal processing in transmission line metamaterial structures. *Radioengineering* **18**, 155–167 (2009).
31. Alu, A., Bilotti, F., Engheta, N. & Vegni, L. Theory and simulations of conformal omnidirectional sub-wavelength metamaterial leaky-wave antenna. *IEEE Trans. Ant. Propagat.* **55**, 1698–1708 (2007).
32. Lier, E., Werner, D. H., Scarborough, C. P., Wu, Q. & Bossard, J. A. An octave-bandwidth negligible-loss radiofrequency metamaterial. *Nat. Mater.* **10**, 216–222 (2011).
33. Jiang, Z. H., Gregory, M. D. & Werner, D. H. Experimental demonstration of a broadband transformation optics lens for highly directive multibeam emission. *Phys. Rev. B* **84**, 165111 (2011).
34. Jiang, Z. H., Wu, Q. & Werner, D. H. Demonstration of enhanced broadband unidirectional electromagnetic radiation enabled by a subwavelength profile leaky anisotropic zero-index metamaterial coating. *Phys. Rev. B* **86**, 125131 (2012).
35. Oughstun, K. E. & Shen, S. Dispersive pulse propagation in a double-resonance Lorentz medium. *J. Opt. Soc. Am. B* **5**, 2395–2398 (1988).
36. Dolling, G., Enkrich, C., Wegener, M., Soukoulis, C. M. & Linden, S. Simultaneous negative phase and group velocity of light in a metamaterial. *Science* **312**, 892–894 (2006).
37. Paul, T., Menzel, C., Rockstuhl, C. & Lederer, F. Advanced optical metamaterials. *Adv. Mater.* **22**, 2354–2357 (2010).
38. Haupt, R. L. & Werner, D. H. *Genetic Algorithms in Electromagnetics* (Wiley, 2007).
39. Tang, Y., Bossard, J. A., Werner, D. H. & Mayer, T. S. Single-layer metallodielectric nanostructures as dual-band midinfrared filters. *Appl. Phys. Lett.* **92**, 263106 (2008).
40. ANSYS, *High Frequency Structure Simulator, v12.1*, Ansoft Corporation, Pittsburgh, PA, United States (2010).
41. Smith, D. R., Schultz, S. & Soukoulis, C. M. Determination of effective permittivity and permeability of metamaterials from reflection and transmission coefficients. *Phys. Rev. B* **65**, 195104 (2002).
42. Zhao, Y., Belkin, M. A. & Alù, A. Twisted optical metamaterials for planarized ultrathin broadband circular polarizers. *Nat. Commun.* **3**, 870 (2012).
43. Liu, N. *et al.* Three-dimensional photonic metamaterials at optical frequencies. *Nat. Mater.* **7**, 31–37 (2007).
44. Gansel, J. K. *et al.* Gold helix photonic metamaterial as broadband circular polarizer. *Science* **325**, 1513–1515 (2009).
45. Yeh, P. *Optical Waves in Layered Media* (John Wiley & Sons, 2005).
46. Dolling, G., Wegener, M., Soukoulis, C. M. & Linden, S. Negative-index metamaterial at 780 nm wavelength. *Opt. Lett.* **32**, 53–55 (2007).
47. Zhang, S. *et al.* Demonstration of near-infrared negative-index materials. *Phys. Rev. Lett.* **95**, 137404 (2005).
48. Xiao, S. *et al.* Loss-free and active optical negative-index metamaterials. *Nature* **466**, 735–738 (2010).
49. Xu, T., Wu, Y.-K., Luo, X. & Guo, L. J. Plasmonic nanoresonators for high-resolution colour filtering and spectral imaging. *Nat. Commun.* **1**, 59 (2010).
50. Simovski, C. R. & Tretyakov, S. A. Local constitutive parameters of metamaterials from an effective-medium perspective. *Phys. Rev. B* **75**, 195111 (2007).
51. Koschny, T. H. *et al.* Impact of inherent periodic structure on effective medium description of left-handed and related metamaterials. *Phys. Rev. B* **71**, 245105 (2005).
52. Starr, A. F., Rye, P. M., Smith, D. R. & Nemat-Nasser, S. Fabrication and characterization of a negative-refractive-index composite metamaterial. *Phys. Rev. B* **70**, 113102 (2004).
53. Yang, J., Sauvan, C., Liu, H. T. & Lalanne, P. Theory of fishnet negative-index optical metamaterials. *Phys. Rev. Lett.* **107**, 043903 (2008).
54. Ginzburg, P., Berkovitch, N., Nevet, A., Shor, I. & Orenstein, M. Resonances on-demand for plasmonic nano-particles. *Nano Lett.* **11**, 2329–2333 (2011).
55. Powell, D. A. & Kivshar, Y. S. Substrate-induced bianisotropy in metamaterials. *Appl. Phys. Lett.* **97**, 091106 (2010).
56. Ku, Z. & Brueck, S. R. J. Experimental demonstration of sidewall angle induced bianisotropy in multiple layer negative index metamaterials. *Appl. Phys. Lett.* **94**, 153107 (2009).
57. Chanda, D. *et al.* Large-scale flexible 3D optical negative index metamaterial formed by nanotransfer printing. *Nat. Nanotech.* **6**, 402–407 (2011).

Acknowledgement

This work was supported by the NSF MRSEC Grant No. DMR-0820404. The metamaterial filters were fabricated at the Penn State NSF NNIN site. We thank Philip Gorman for assistance and discussion during the preparation of the manuscript.

Author contributions

Z.H.J. conceived the idea of using deep-subwavelength nano-notches for dispersion tailoring. Z.H.J., S.Y. and D.H.W. contributed to the filter application of the metamaterial. Z.H.J. designed the metamaterial and performed numerical analysis. S.Y. and L.L. fabricated the sample. S.Y., L.L. and Z.H.J. performed optical characterization and analyzed the data. D.H.W. and T.S.M. supervised the project. All authors co-wrote the manuscript.

Additional information

Supplementary information accompanies this paper at <http://www.nature.com/scientificreports>

Competing financial interests: The authors declare no competing financial interests.

License: This work is licensed under a Creative Commons Attribution-NonCommercial-NoDerivs 3.0 Unported License. To view a copy of this license, visit <http://creativecommons.org/licenses/by-nc-nd/3.0/>

How to cite this article: Jiang, Z.H. *et al.* Tailoring Dispersion for Broadband Low-loss Optical Metamaterials Using Deep-subwavelength Inclusions. *Sci. Rep.* **3**, 1571; DOI:10.1038/srep01571 (2013).